

# Measurement of quantum back action in the audio band at room temperature

Jonathan Cripe<sup>1\*</sup>, Nancy Aggarwal<sup>2</sup>, Robert Lanza<sup>2</sup>, Adam Libson<sup>2</sup>, Robinjeet Singh<sup>1</sup>, Paula Heu<sup>3,4</sup>, David Follman<sup>3,4</sup>, Garrett D. Cole<sup>3,4,5</sup>, Nergis Mavalvala<sup>2</sup> & Thomas Corbitt<sup>1\*</sup>

**Quantum mechanics places a fundamental limit on the precision of continuous measurements. The Heisenberg uncertainty principle dictates that as the precision of a measurement of an observable (for example, position) increases, back action creates increased uncertainty in the conjugate variable (for example, momentum). In interferometric gravitational-wave detectors, higher laser powers reduce the position uncertainty created by shot noise (the photon-counting error caused by the quantum nature of the laser) but necessarily do so at the expense of back action in the form of quantum radiation pressure noise (QRPN)<sup>1</sup>. Once at design sensitivity, the gravitational-wave detectors Advanced LIGO<sup>2</sup>, VIRGO<sup>3</sup> and KAGRA<sup>4</sup> will be limited by QRPN at frequencies between 10 hertz and 100 hertz. There exist several proposals to improve the sensitivity of gravitational-wave detectors by mitigating QRPN<sup>5–10</sup>, but until now no platform has allowed for experimental tests of these ideas. Here we present a broadband measurement of QRPN at room temperature at frequencies relevant to gravitational-wave detectors. The noise spectrum obtained shows effects due to QRPN between about 2 kilohertz and 100 kilohertz, and the measured magnitude of QRPN agrees with our model. We now have a testbed for studying techniques with which to mitigate quantum back action, such as variational readout and squeezed light injection<sup>7</sup>, with the aim of improving the sensitivity of future gravitational-wave detectors.**

Gravitational-wave (GW) detectors such as Advanced LIGO continuously monitor the position of test masses using electromagnetic radiation. The Heisenberg uncertainty principle limits the precision of such a continuous measurement owing to the quantization of light. Uncertainty in the number of photons reflecting from a mirror exerts a fluctuating force due to radiation pressure on the mirror, causing mechanical motion<sup>1,11,12</sup>. This force leads to a noise source for GW measurements, namely, QRPN. GW interferometers typically use as much laser power as possible in order to minimize the shot noise and maximize the signal-to-noise ratio for GWs. Advanced LIGO and other second and third generation interferometers will be limited by QRPN at low frequency when running at their full laser power.

Given the imperative for more-sensitive GW detectors, it is important to study the effects of QRPN in a system similar to Advanced LIGO, which will be limited by QRPN across a wide range of frequencies far from the mechanical resonance frequency of the test mass suspension. Studying quantum mechanical motion is challenging, however, owing to the fact that classical noise sources such as environmental vibrations and thermally driven fluctuations<sup>13</sup> usually dominate over quantum effects. Previous observations of QRPN have observed such subtle quantum effects, even at room temperature, but these experiments have thus far been limited to high frequencies (megahertz to gigahertz) and in a narrow band around a mechanical resonance<sup>14–17</sup>.

In this work, we present a broadband and off-resonance measurement of QRPN in the audio frequency band. We have developed low-loss single-crystal microresonators with sufficiently minimized

thermal noise that the quantum effects can be observed at room temperature. The optomechanical system, shown in detail in Fig. 1, is a Fabry–Pérot cavity with a mechanical oscillator as one of the cavity mirrors. The optomechanical cavity is just under 1 cm long and consists of a high-reflectivity single-crystal microresonator that serves as the input coupler and a macroscopic mirror with a 1-cm radius of curvature as the back reflector. The cavity is made slightly shorter than the 1-cm radius of curvature of the large mirror in order to achieve a small spot size on the microresonator while maintaining stable cavity modes. The microresonator consists of a roughly 70- $\mu\text{m}$ -diameter mirror pad suspended from a single-crystal GaAs cantilever with a thickness of 220 nm, a width of 8  $\mu\text{m}$  and a length of 55  $\mu\text{m}$ . The mirror pad is made up of 23 pairs of quarter-wave optical thickness GaAs/Al<sub>0.92</sub>Ga<sub>0.08</sub>As layers for a transmission of 250 parts per million (p.p.m.) and exhibits both low optical losses and a high mechanical quality factor<sup>18–21</sup>. The microresonator has a mass of 50 ng, a natural mechanical frequency of 876 Hz and a measured mechanical quality factor of 16,000 at room temperature (295 K). The cavity has a finesse of 13,000 and half-width at half-maximum (HWHM) linewidth of 580 kHz.

A 1,064 nm Nd:YAG laser beam is used to both stabilize the optomechanical cavity and measure the mechanical motion of the microresonator. The cavity is detuned from resonance by 0.3 to 0.6 linewidths, and locked using a feedback loop that utilizes the restoring force produced by a strong optical spring<sup>22</sup>, which shifts the mechanical resonance of the microresonator up to 145 kHz at high power. We choose to detune the cavity primarily because it is nearly impossible to avoid a strong optical-spring effect owing to the weak restoring force provided by the cantilever supporting the microresonator. We would need to keep the cavity locked to resonance within  $2 \times 10^{-5}$  linewidths, or about 10 Hz, to avoid having an optical spring as stiff as the cantilever, and any deviations around this point would produce strong variations in the optical-spring stiffness. Instead, by intentionally detuning the cavity by nearly 0.5 linewidths, we operate near the peak optical-spring stiffness, where the cavity is relatively insensitive to variations in detuning, as described in Methods. The error signal for the feedback loop is detected using photodetector PD<sub>L</sub> in transmission of the cavity and photodetector PD<sub>M</sub> in reflection. The error signal is fed back to an amplitude and phase modulator, as shown in Fig. 1.

The final measurement configuration uses only the reflected light because the transmitted light has relatively large shot noise due to the small transmission (50 p.p.m.) of the end mirror, which may pollute the measurement. Reflection locking with the phase modulator is less robust, and we are not able to acquire lock directly without first using the transmission locking and amplitude modulator. We measure the displacement noise spectrum by detecting the light that is reflected from the cavity. After the cavity is locked, the signal from PD<sub>M</sub> is sent to a spectrum analyser for analysis. We measure an uncalibrated noise spectrum by first measuring the amplitude spectral density of the output from PD<sub>M</sub>. We calibrate the spectrum by dividing it by the transfer function from the laser-cavity piezo to PD<sub>M</sub>. This method treats the

<sup>1</sup>Department of Physics and Astronomy, Louisiana State University, Baton Rouge, LA, USA. <sup>2</sup>LIGO–Massachusetts Institute of Technology, Cambridge, MA, USA. <sup>3</sup>Crystalline Mirror Solutions LLC, Santa Barbara, CA, USA. <sup>4</sup>Crystalline Mirror Solutions GmbH, Vienna, Austria. <sup>5</sup>Vienna Center for Quantum Science and Technology (VCQ), Faculty of Physics, University of Vienna, Vienna, Austria. \*e-mail: jcripe1@lsu.edu; tcorbitt@phys.lsu.edu

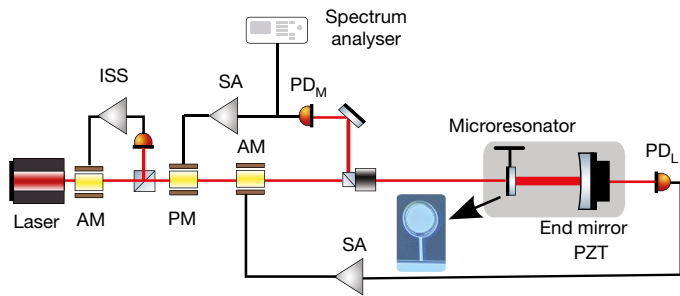


**Fig. 1 | Experimental set-up.** Laser light passes through an amplitude modulator (AM), phase modulator (PM) and a second AM before entering the cavity, which sits on a suspended platform inside a vacuum chamber (shown in grey). The optomechanical cavity consists of a microresonator (shown in the inset) and a macroscopic mirror mounted on a piezoelectric transducer (PZT). An intensity stabilization servo (ISS) is used to minimize classical intensity fluctuations and stabilize the laser power to shot noise. The transmission (reflection) is detected by photodetector  $PD_L$  ( $PD_M$ ) and passed through a servo amplifier (SA) before being sent to the AM (PM) for feedback. The cavity is initially locked using  $PD_L$ , but is switched to using  $PD_M$  for the final measurement.

optical spring as a feedback loop<sup>22</sup>, and by factoring out its effect, we restore the observed displacement spectrum to what it would be in the absence of the optical spring and our electronic feedback. The laser piezo has been calibrated in frequency, which allows the resulting signal to be calibrated to displacement by using the cavity length.

To understand the resulting measurement of the microresonator motion, we must carefully account for various noise sources. Specifically, we consider QRPN, thermal noise, shot noise, dark noise of the photodiode readout, and classical intensity and frequency fluctuations of the laser. Thermal noise, governed by the fluctuation dissipation theorem, sets a limit on the precision of force and displacement measurements<sup>23</sup>, and is also one of the main limitations in this experiment. We rely on direct measurements of thermal noise to quantify its effects. To measure thermal noise, we operate the cavity with about 10 mW of circulating power, a level at which the QRPN is small compared to the Brownian motion of the microresonator. One challenge in accurately accounting for the thermal noise is that as the circulating power in the cavity is increased, the beam position on the microresonator shifts slightly, and the coupling of the pitch and yaw modes of the microresonator changes. To account for this, we measure the thermal noise at different alignments with 10 mW of circulating power to match the desired alignment at higher power, and ultimately use these

measurements to constrain a model. The measured thermal data are used at most frequencies, except those near the pitch, yaw and side-to-side resonances, as described in Methods. The observed thermal noise agrees with a structural damping model<sup>13,24</sup> from 200 Hz to 30 kHz. Modelled thermal noise ( $\tilde{x}_{th}$ ) is used near the resonances because it is difficult to reproduce the exact alignment at low and high powers. Structural damping models contain a frequency-independent loss angle, and for a harmonic oscillator have a displacement amplitude spectral density of

$$\tilde{x}_{th}(\omega) = \sqrt{\frac{4k_B T \omega_m^2}{\omega m Q [(\omega_m^2 - \omega^2)^2 + \frac{\omega_m^4}{Q^2]}}}$$
 (1)

where  $k_B$  is the Boltzmann constant,  $T$  is temperature,  $m$  is mass,  $Q$  is the quality factor,  $\omega = 2\pi f$ , where  $f$  is the measurement frequency, and  $\omega_m$  is the angular frequency of the mechanical mode<sup>13</sup>. Above 30 kHz, we observe thermal noise that deviates from the structural damping model, which appears to be consistent with thermoelastic damping of the drumhead mode of the microresonator. In the noise budget, we use the measured thermal noise at these frequencies. The resulting thermal noise, which is used in our noise budget, is shown in Fig. 2.

Quantum noise is the other dominant noise source in the experiment, and we use an input–output model for comparison to our measurements. The model calculates quantum noise using a set of equations that relate the output fields to the input fields<sup>25,26</sup>. The model requires knowledge of the optical losses, detuning and the power circulating in the cavity, in addition to the microresonator’s mechanical susceptibility. The cavity losses, detuning and circulating power are constrained by measurements of the optical spring. The parameters for the microresonator are constrained by the thermal noise measurement. The details of these measurements are presented in Methods, along with analysis of the effects of uncertainty in these parameters. The model then predicts the level of QRPN, as shown in Fig. 2 for 220 mW of circulating power. To further verify the model of QRPN, we also measure the response of our system to intensity fluctuations of the input laser beam, multiply that measurement with the level of shot noise for the input power, and calibrate the resulting projected noise level. This results in an independent measurement for the level of QRPN that agrees with the modelled result. The details of the measurement are presented in Methods.

In order to observe quantum back action, we measure the cavity displacement noise at five cavity circulating powers of 10 mW, 73 mW,

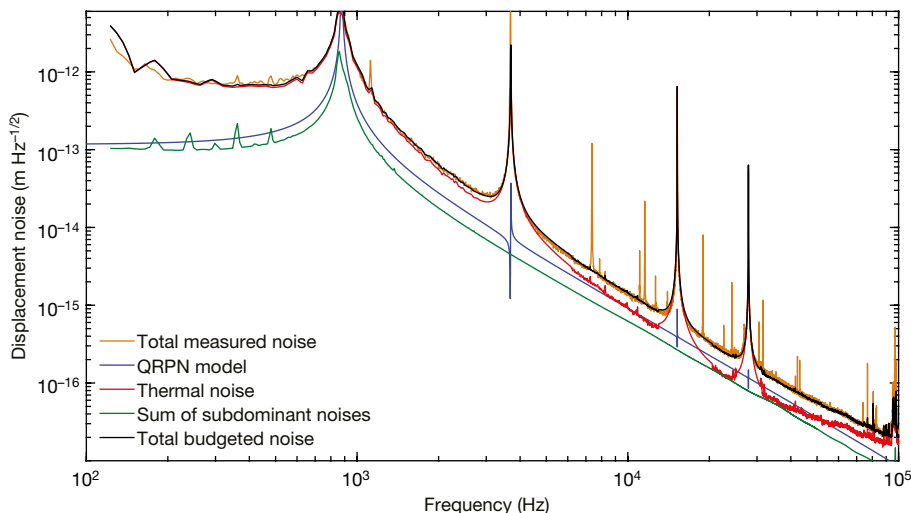


**Fig. 2 | Measured and budgeted noise.** Contributions of various noise sources to the displacement of the microresonator, shown as amplitude spectral densities, are shown for the case with 220 mW circulating

power. The resonances at 3.7 kHz, 15 kHz and 28 kHz are higher-order mechanical modes of the microresonator. Each of these noise sources (see key) is discussed in detail in Methods and in Extended Data Fig. 1.

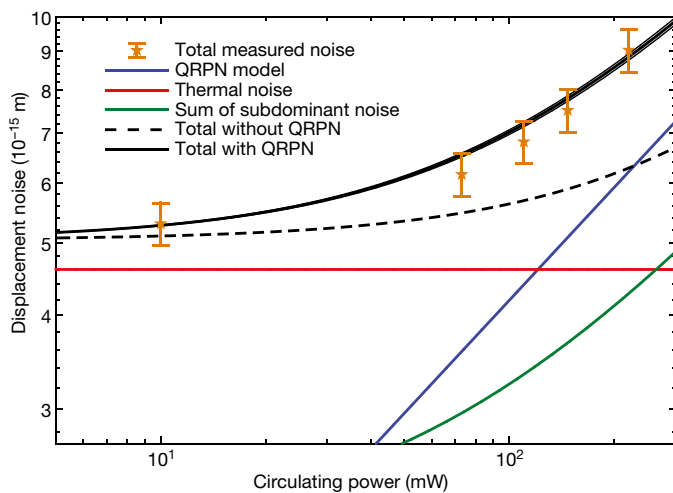


**Fig. 3 | Power scaling.** Five measurements at circulating powers of 10 mW, 73 mW, 110 mW, 150 mW and 220 mW show how each of the noise sources scales with cavity circulating power. Each noise source is integrated between 21 kHz and 22 kHz. Error bars on the measured data represent statistical uncertainty (s.d.). The dashed black curve is the expected total noise without including the contribution from QRPN. The shaded grey region around the black curve represents the uncertainty in the total displacement noise due to uncertainty in the level of QRPN from the model.

110 mW, 150 mW and 220 mW. For each power level, the input power is multiplied by the same factor. Owing to the shifting alignment resulting from static radiation pressure, the optical losses in the cavity change as a function of power. This effect is quantified through measurements of the optical spring. The detuning varies from about 0.6 to 0.35 linewidths when going from low to high power, but this only affects the level of QRPN by  $\pm 4\%$ , as explained in Methods. The measured noise at 220 mW, shown as the orange curve in Fig. 2, shows that the measured noise agrees with the sum of all known noise sources. Below 10 kHz, thermal noise is the biggest contributor to the displacement noise, but the effect of QRPN is still visible in the displacement noise measurement down to 2 kHz, where it accounts for about 20% of the measured displacement noise. The measured classical radiation pressure noise from classical intensity fluctuations of the laser and laser frequency noise<sup>27</sup> are below the other noise sources across the measurement band, as shown in Extended Data Fig. 1.

To demonstrate that the observed QRPN scales with the expected square root of power<sup>1</sup>, we compare the noise at each power level. The data are shown in Fig. 3, where the displacement noise spectrum has been integrated over a 1 kHz band between 21 kHz and 22 kHz. The observed data are consistent with the predicted scaling, and the QRPN is the largest noise source for circulating powers above 150 mW. For the measurement at 220 mW shown in Fig. 3, QRPN represents 48% of the total noise, while the thermal noise accounts for 27%, with the remaining 25% composed of the sum of the subdominant noise sources. We sum in quadrature the contribution of each of the noise sources to compute the total expected noise. We find that our five displacement noise measurements, shown as orange stars in Fig. 3, agree with the total expected noise (black curve) with the statistical measurement error taken into account. The measurement error is calculated by repeating the measurement multiple times and is dominated by the fluctuations in the transfer function measurement that is used to calibrate the spectrum. The dashed black curve shown in Fig. 3 is the predicted displacement noise without a contribution from QRPN. The measurements of the displacement noise rule out the model without QRPN.

In addition to showing that the noise scales correctly with optical power, a variety of other tests were performed to further verify that that we are observing QRPN. First, we put constraints on shot noise, dark noise, and classical laser intensity and frequency noise, as seen in

Extended Data Fig. 1. Second, we fit the noise we attribute to QRPN to a power law in frequency, and require the resulting fit to match the measured data to within 10% in the 1–100 kHz frequency range. The resulting frequency scaling ( $f^{-1.95 \pm 0.2}$ ) matches the expected frequency dependence ( $f^{-2}$ ), and excludes the frequency dependence of thermal noise ( $f^{-5/2}$ ). Third, we also rule out that this could be an effect of excess bulk heating of the microresonator by verifying that the thermal noise at low frequencies remains the same within  $\pm 2\%$  measurement uncertainties (see Methods). Using the optical-spring measurement to constrain the cavity losses also allows us to rule out absorption photothermal effects<sup>28</sup> because any excess damping would be observed in mechanical response measurements. Finally, we perform a transfer function measurement by amplitude modulating the input light and measuring the response at PD<sub>M</sub>. By comparing to a similar transfer function while the cavity is far from resonance, we show that the cavity coherently amplifies the amplitude modulations, indicating the presence of an optomechanical parametric process. Additionally, we can project the expected level of QRPN by multiplying this transfer function with the magnitude of the vacuum fluctuations that enter the cavity, and dividing by our calibration transfer function. We find that this projection matches the QRPN model.

Since the first proposals of interferometric GW detectors, QRPN has been known to present a fundamental limit to the low-frequency sensitivity of GW detectors. For the past two decades, the measurement of QRPN at frequencies relevant for GW detectors has eluded increasingly sensitive experiments. The presented ability to measure QRPN at frequencies in the GW band opens up the possibility of experimental tests of QRPN-reduction schemes<sup>5–10</sup>. This ability has already led to measurements of ponderomotive squeezing<sup>29</sup>, cancellation of QRPN<sup>30</sup>, and the suppression and amplification of QRPN with squeezed light<sup>31</sup>. From a fundamental standpoint, the measurement of QRPN amounts to observation of quantum vacuum fluctuations inducing motion of a macroscopic object.

### Online content

Any methods, additional references, Nature Research reporting summaries, source data, statements of data availability and associated accession codes are available at <https://doi.org/10.1038/s41586-019-1051-4>.

Received: 11 April 2018; Accepted: 15 January 2019;

Published online: 25 March 2019

1. Caves, C. M. Quantum-mechanical radiation-pressure fluctuations in an interferometer. *Phys. Rev. Lett.* **45**, 75–79 (1980).
2. The LIGO Scientific Collaboration. Advanced LIGO. *Class. Quantum Gravity* **32**, 074001 (2015).
3. Acernese, F. et al. Advanced Virgo: a second-generation interferometric gravitational wave detector. *Class. Quantum Gravity* **32**, 024001 (2015).
4. Somiya, K. Detector configuration of KAGRA—the Japanese cryogenic gravitational-wave detector. *Class. Quantum Gravity* **29**, 124007 (2012).
5. Braginsky, V. B., Vorontsov, Y. I. & Thorne, K. S. Quantum nondemolition measurements. *Science* **209**, 547–557 (1980).
6. Braginsky, V. B., Gorodetsky, M. L., Khalili, F. Y. & Thorne, K. S. Dual-resonator speed meter for a free test mass. *Phys. Rev. D* **61**, 044002 (2000).
7. Kimble, H. J., Levin, Y., Matsko, A. B., Thorne, K. S. & Vyatchanin, S. P. Conversion of conventional gravitational-wave interferometers into quantum nondemolition interferometers by modifying their input and/or output optics. *Phys. Rev. D* **65**, 022002 (2001).
8. Harms, J. et al. Squeezed-input, optical-spring, signal-recycled gravitational-wave detectors. *Phys. Rev. D* **68**, 042001 (2003).
9. Oelker, E. et al. Audio-band frequency-dependent squeezing for gravitational-wave detectors. *Phys. Rev. Lett.* **116**, 041102 (2016).
10. Gräf, C. et al. Design of a speed meter interferometer proof-of-principle experiment. *Class. Quantum Gravity* **31**, 215009 (2014).
11. Braginsky, V. B. & Manukin, A. B. *Measurement of Weak Forces in Physics Experiments* (Univ. Chicago Press, Chicago, 1977).
12. Caves, C. M. Quantum-mechanical noise in an interferometer. *Phys. Rev. D* **23**, 1693–1708 (1981).
13. Saulson, P. R. Thermal noise in mechanical experiments. *Phys. Rev. D* **42**, 2437–2445 (1990).
14. Purdy, T. P., Peterson, R. W. & Regal, C. A. Observation of radiation pressure shot noise on a macroscopic object. *Science* **339**, 801–804 (2013).
15. Teufel, J. D., Lecocq, F. & Simmonds, R. W. Overwhelming thermomechanical motion with microwave radiation pressure shot noise. *Phys. Rev. Lett.* **116**, 013602 (2016).

16. Purdy, T. P., Grutter, K. E., Srinivasan, K. & Taylor, J. M. Quantum correlations from a room-temperature optomechanical cavity. *Science* **356**, 1265–1268 (2017).
17. Sudhir, V. et al. Quantum correlations of light from a room-temperature mechanical oscillator. *Phys. Rev. X* **7**, 031055 (2017).
18. Cole, G. D., Gröblacher, S., Gugler, K., Gigan, S. & Aspelmeyer, M. Monocrystalline Al<sub>x</sub>Ga<sub>1-x</sub>As heterostructures for high-reflectivity high-Q micromechanical resonators in the megahertz regime. *Appl. Phys. Lett.* **92**, 261108 (2008).
19. Cole, G. D. Cavity optomechanics with low-noise crystalline mirrors. *Proc. SPIE* **8458**, 845807 (2012).
20. Cole, G. D. et al. High-performance near- and mid-infrared crystalline coatings. *Optica* **3**, 647–656 (2016).
21. Singh, R., Cole, G. D., Cripe, J. & Corbitt, T. Stable optical trap from a single optical field utilizing birefringence. *Phys. Rev. Lett.* **117**, 213604 (2016).
22. Cripe, J. et al. Radiation-pressure-mediated control of an optomechanical cavity. *Phys. Rev. A* **97**, 013827 (2018).
23. Nyquist, H. Thermal agitation of electric charge in conductors. *Phys. Rev.* **32**, 110–113 (1928).
24. Fedorov, S. et al. Evidence for structural damping in a high-stress silicon nitride nanobeam and its implications for quantum optomechanics. *Phys. Lett. A* **382**, 2251–2255 (2018).
25. Corbitt, T., Chen, Y. & Mavalvala, N. Mathematical framework for simulation of quantum fields in complex interferometers using the two-photon formalism. *Phys. Rev. A* **72**, 013818 (2005).
26. Corbitt, T. et al. Squeezed-state source using radiation-pressure-induced rigidity. *Phys. Rev. A* **73**, 023801 (2006).
27. Willke, B., Brozek, S., Danzmann, K., Quetschke, V. & Gossler, S. Frequency stabilization of a monolithic Nd:YAG ring laser by controlling the power of the laser-diode pump source. *Opt. Lett.* **25**, 1019–1021 (2000).
28. Braginsky, V., Gorodetsky, M. & Vyatchanin, S. Thermodynamical fluctuations and photo-thermal shot noise in gravitational wave antennae. *Phys. Lett. A* **264**, 1–10 (1999).
29. Aggarwal, N. et al. Room temperature optomechanical squeezing. Preprint at <http://arXiv.org/abs/1812.09942> (2018).
30. Cripe, J. et al. Quantum back action cancellation in the audio band. Preprint at <http://arXiv.org/abs/1812.10028> (2018).
31. Yap, M. J. et al. Broadband reduction of quantum radiation pressure noise via squeezed light injection. Preprint at <http://arXiv.org/abs/1812.09804> (2018).

**Acknowledgements** J.C. and T.C. are supported by National Science Foundation grants PHY-1150531 and PHY-1806634. N.A., A.L. and N.M. are supported by National Science Foundation grants PHY-1707840 and PHY-1404245. A portion of this work was performed in the UCSB Nanofabrication Facility. J.C. and T.C. thank D. McClelland, R. Ward and M. J. Yap for comments and discussion. The authors thank C. Wipf and V. Sudhir for comments during the manuscript preparation. This document has been assigned the LIGO document number LIGO-P1800033.

**Reviewer information** *Nature* thanks Warwick Bowen, Yuta Michimura and the other anonymous reviewer(s) for their contribution to the peer review of this work.

**Author contributions** J.C. led the design, construction and data taking for the experiment, and prepared the manuscript. T.C. supervised the design and construction of the experiment, and also helped with the data taking and analysis of the results. N.A., R.L., A.L. and N.M. contributed to the design of the microresonators and the writing of the manuscript. G.D.C. provided feedback on the design of the microresonators and, together with P.H. and D.F., fabricated the devices. R.S. contributed experience from previous experiments.

**Competing interests** The authors declare no competing interests.

#### Additional information

**Extended data** is available for this paper at <https://doi.org/10.1038/s41586-019-1051-4>.

**Reprints and permissions information** is available at <http://www.nature.com/reprints>.

**Correspondence and requests for materials** should be addressed to J.C. or T.C. **Publisher's note:** Springer Nature remains neutral with regard to jurisdictional claims in published maps and institutional affiliations.

© The Author(s), under exclusive licence to Springer Nature Limited 2019



## METHODS

**Noise budget.** In addition to the QRPN and thermal noise shown in Fig. 2, subdominant noise sources contribute to the measured displacement noise spectrum. A full noise budget for the 220 mW measurement is shown in Extended Data Fig. 1. The largest of the subdominant noise sources is the combination of shot noise and dark noise that is present on  $PD_M$ . Extended Data Fig. 1 includes a measurement of the combined shot noise and dark noise. Factoring out the effect of the optical spring using the calibration discussed in the main text causes the white shot noise to have the frequency dependence shown in Extended Data Fig. 1. Classical laser intensity noise and laser frequency noise lie below the other noise sources. Extended Data Fig. 1 includes our measurement of the classical laser intensity noise and laser frequency noise level for the Nd:YAG ring laser<sup>27</sup>.

With all of the noise sources accounted for, we find that QRPN is the dominant noise source over a wide range of frequencies with 220 mW of light circulating in the cavity, as seen in Fig. 2 and Extended Data Fig. 1. To quantify the effect of QRPN across our measurement band as a function of power, we provide a contour plot showing the ratio of QRPN to the total measured displacement noise in Extended Data Fig. 5.

**Thermal noise.** As described in the main text, thermal noise sets a limit on the precision of mechanical experiments and can overwhelm attempts to measure quantum effects if it is too large. As one of the principal noise sources in this experiment, we must measure the thermal noise across our measurement band and account for it in our noise budget analysis. One difficulty in accounting for the thermal noise is that the cavity alignment shifts slightly as the circulating power is increased and the cantilever is deflected by radiation pressure. Even a small change in alignment can change the coupling of higher-order mechanical modes, specifically the yaw, pitch and side-to-side modes, as shown in Extended Data Fig. 2.

We model the thermal noise using a finite element model of the microresonator that is based on dimensions obtained from a micrograph of the resonator and is further constrained by measurements of the frequencies and quality factors of the fundamental mode and the next three higher-order modes. We include the material properties of the GaAs and AlGaAs (such as density, Young's modulus, anisotropy, and so on) in the model. The total thermal noise spectrum is then calculated using equation (1) by summing the contribution of each mechanical mode in quadrature as<sup>13</sup>

$$\tilde{x}_{th}^2(\omega) = \sum_i \frac{4k_B T \omega_i^2}{\omega m_i Q_i \left[ (\omega_i^2 - \omega^2)^2 + \frac{\omega_m^4}{Q_i^2} \right]} \quad (2)$$

where  $\omega_i$ ,  $Q_i$  and  $m_i$  are the resonance frequency, quality factor and mass of each mode. We infer the modal mass for each mode by using the thermal noise measurement presented below, and are able to reproduce the inferred modal masses by changing the beam position in the finite element model.

The thermal noise curve shown in Fig. 2 in the main text is a combination of a measurement at frequencies away from the higher-order mechanical modes and a model at frequencies around the yaw, pitch and side-to-side modes. The modelled thermal noise is used around the mechanical modes because the thermal noise must be measured at a low circulating power of 10 mW, and it is difficult to reproduce precisely the same alignment at different power levels. The modal mass of the higher-order modes is set in the model by comparing the magnitude and width of the higher-order mode resonance peaks in the displacement noise measurement shown in orange in Fig. 2 with those in the model, at frequencies dominated by thermal noise.

In order to demonstrate that the slight changes in alignment resulting from high circulating power do not introduce excess thermal or technical noise that could mask the effect of QRPN, we measure the displacement noise at 10 mW circulating power with the microresonator position shifted to be as close as possible to the alignment with 220 mW of circulating power, as determined by the observed peak height and width of the pitch and yaw modes. By comparing the results of that measurement with thermal noise measurements in the nominal alignment at lower power, shown in Extended Data Fig. 3, we confirm that the thermal noise at frequencies away from the resonances is consistent with the model for structural damping ( $f^{-5/2}$ ) and does not change in a way that is consistent with the observed QRPN ( $f^{-2}$ ). Producing a thermal noise level at 20 kHz that would be as large as QRPN would require thermal noise with a frequency dependence inconsistent with our observed data in Extended Data Fig. 3. Further, the degree of misalignment necessary would introduce cavity losses much greater than observed.

**Calibration and uncertainties.** In order to properly model the expected level of QRPN, we must know key properties of the mechanical and optical system, specifically the mass of the microresonator, the power circulating in the cavity, the total optical losses in the cavity, the length of the cavity and its detuning from resonance. In this section, we describe how these quantities are measured, and the effects of uncertainty in those measurements.

The mass of the microresonator is measured to within  $\pm 10\%$  using the measured thermal noise spectrum shown in Extended Data Fig. 3 at frequencies near the fundamental resonance. The thermal noise, given in equation (1), depends on the temperature, mechanical resonance frequency, quality factor and mass. The temperature is well known, and there is insignificant heating of the cantilever with the small circulating power used in measuring the thermal noise. The mechanical resonance frequency and quality factor are measured to good precision using ringdown measurements with an optical lever set-up. Therefore, we may use the thermal noise measurements to constrain the mass of the microresonator to 50 ng. The estimated  $\pm 10\%$  uncertainty is associated with systematic uncertainties arising in calibrating the measured thermal noise. The measured mass is consistent with a finite element model of the microresonator based on measured dimensions of the microresonator that are determined from a micrograph.

The cavity length is constrained by measurements of the geometric size of the cavity mode. Given the known radius of curvature of the back reflector mirror ( $1 \text{ cm} \pm 100 \mu\text{m}$ ), the stability of the cavity puts an upper limit on the cavity length. We further constrain the cavity length by measuring the size of the cavity mode, which is imaged with a camera, and conclude that the overall cavity length must be within  $100 \mu\text{m}$  of the radius of curvature of the reflector. Using this method, we conclude our cavity length is within  $200 \mu\text{m}$  of 1 cm.

To constrain the optical parameters, we have found using measurements of the optical spring to be the most accurate technique. To measure the optical spring, we measure the frequency-dependent optical response of the system amplitude modulating the light injected into the cavity using the second amplitude modulator, as shown in Fig. 1. We measure a swept sine transfer function between the injected modulation and the modulation detected in transmission of the cavity at  $PD_L$  before the feedback is switched to the phase modulator. This provides a clear measurement of the optical-spring frequency and damping<sup>22</sup>.

To obtain the other parameters, we first hold the power incident on the cavity constant, while varying the cavity length by tuning the cavity piezo. By performing an optical-spring measurement at each setting, we may find the cavity length and transmitted power level (as measured by  $PD_L$ ) that has the highest-frequency optical spring. This allows us to set the detuning to a known value of 0.6 with an accuracy of  $\pm 7\%$  for these settings, corresponding to a maximum in the optical-spring constant<sup>32</sup>

$$K(\omega) = \frac{32\pi P_{\text{circ}}}{c\lambda_0 T_{\text{total}}} \frac{\delta_\gamma}{1 + \delta_\gamma} \times \frac{1 + \delta_\gamma^2 - (\omega/\gamma)^2}{[1 + \delta_\gamma^2 - (\omega/\gamma)^2]^2 + 4(\omega/\gamma)^2} \quad (3)$$

where  $P_{\text{circ}}$  is the circulating power in the cavity,  $c$  is the speed of light in vacuum,  $T_{\text{total}}$  is the fraction of light leaving the cavity in one round trip (including loss and mirror transmission),  $\lambda_0$  is the laser wavelength,  $\delta_\gamma$  is the detuning of the cavity in units of the HWHM linewidth  $\gamma$ , and  $\omega$  is the measurement frequency. This method is independent of knowledge of the optical power level and cavity losses.

Once the detuning is determined by the above method, we then constrain the circulating power and cavity losses by matching the optical-spring frequency and quality factor using the measured transfer function of the optical response. This is possible because, while the real ( $K$ ) and imaginary ( $\Gamma_{\text{OS}}$ ) parts of the optical-spring constant vary identically with circulating power, they do not scale identically with the cavity linewidth<sup>32</sup> (and hence losses), as described by:

$$\Gamma_{\text{OS}}(\omega) = \frac{2K/m}{\gamma[1 + \delta_\gamma^2 - (\omega/\gamma)^2]} \quad (4)$$

Using this method, we constrain the circulating power to be 73 mW with an accuracy of 10% and total cavity losses to 470 p.p.m.  $\pm 10$  p.p.m. The cavity losses are composed of the transmission of the microresonator ( $T_i \approx 250$  p.p.m.) and the transmission of the end mirror ( $T_o \approx 50$  p.p.m.), with the remainder a combination of absorption, scattering and diffraction loss ( $L = 170$  p.p.m.). The observed total loss corresponds to a cavity linewidth of  $560 \text{ kHz} \pm 10 \text{ kHz}$  and is consistent with an independent measurement of the cavity linewidth. The independent measurement was performed by measuring the transfer function of amplitude fluctuations to  $PD_L$  at frequencies between 500 kHz and 10 MHz with the cavity operated at a high detuning.

For the measurements at high circulating power levels, we scaled both the input power and the transmitted power by identical factors. Nominally, one might expect this to keep the cavity detuning constant, but we found that the detuning varied by a small amount. This change in detuning is attributed to the changing alignment of the cavity beam on the microresonator as a result of the larger static radiation pressure as the power is increased. The slight shift in beam position on the microresonator can lead to changes in the cavity losses, probably due to diffraction loss around the edge. This change in losses will in turn be accompanied by a change in detuning in order to maintain the ratio of circulating power to input power. To take this effect into account, we measure the optical-spring transfer function as described above. Since the input power and the transmitted power are now already determined (because they were scaled from the 73 mW circulating power

configuration), the optical detuning and optical losses are varied to match the observed optical-spring transfer function to the model. From this analysis, we determine the cavity detuning to be 0.45 linewidths, 0.43 linewidths and 0.35 linewidths to within  $\pm 6\%$ , and total losses ( $T_{\text{total}} = T_i + T_o + L$ ) to be 490 p.p.m., 495 p.p.m. and 505 p.p.m. to within  $\pm 10$  p.p.m., for circulating power levels of 110 mW, 150 mW and 220 mW, respectively. The total losses correspond to cavity linewidths of 585 kHz  $\pm 10$  kHz, 590 kHz  $\pm 10$  kHz and 600 kHz  $\pm 10$  kHz for circulating power levels of 110 mW, 150 mW and 220 mW, respectively.

We further investigate the effect of uncertainty in the cavity detuning and cavity losses in our measurements and study its effect on the level of modelled QRPN. By holding the transmitted power and input power constant, the level of optical loss determines the required cavity detuning that will match the measurements. In Extended Data Fig. 4 we show the modelled level of QRPN as we vary the loss and detuning for the 220 mW case. With our estimated uncertainties in detuning, we may conclude that the resulting uncertainty in the modelled QRPN is  $\pm 4\%$ , well within our measurement uncertainty.

Our calibration method of using the laser-cavity piezo to measure the response at  $\text{PD}_M$  manifestly removes the effect of the optical spring and our electronic control loop. We calibrate by modulating the laser frequency and measuring its frequency dependent response at  $\text{PD}_M$ . This measurement relies on a change in the laser frequency acting equivalently to a change in cavity length, scaled by the factor  $L/\omega_0$ . Thus, this transfer function directly allows us to measure the effect of a given amount of displacement on our measurement PD, irrespective of the control system. This is equivalent to any experiment that uses feedback control to keep a system near its operational point.

**Comparison to standard cavity optomechanics.** The device used in this experiment may not initially appear to be that useful for quantum cavity optomechanics because of its modest mechanical quality factor and low resonance frequency. In this section, we describe why standard metrics<sup>33</sup> are not effective in our case. We summarize common parameters in Extended Data Table 1. Notably, our system does not satisfy the requirement<sup>14</sup> for observing QRPN that  $(C/n_{\text{th}}) \times [1 + (2\omega_m/\kappa)^2]^{-1} > 1$ , where  $C$  is the multiphoton cooperativity,  $n_{\text{th}}$  is the thermal phonon occupation,  $\omega_m$  is the mechanical resonance frequency, and  $\kappa$  is the FWHM cavity decay rate. This result should not be surprising given that the system is in fact dominated by thermal noise at the bare mechanical resonance frequency, and that these parameters are intended to be relevant in a viscously damped system. It also would not be logical to use the optical-spring parameters in place of the bare mechanical parameters because the region in which we measure is below the optical-spring resonance frequency. This requirement could be modified to account for the observed structural damping as  $C > n_{\text{th}} \times \omega_m/\omega \times [1 + (2\omega_m/\kappa)^2]^{-1}$ , which is satisfied in our system for sufficiently large  $\omega$ .

Here, we illustrate the key parameters of our system that make this measurement possible. The full calculation of quantum noise must include the effect of vacuum fluctuations that enter the system wherever there is a loss. We may simplify this calculation for illustrative purposes by assuming an ideal cavity for which the only loss is the transmission of the microresonator (that is,  $T_{\text{total}} = T_i$ ). To calculate the same level of QRPN as in our real system, we assume the circulating power and cavity decay rate are the same in both cases. For the  $P_{\text{circ}} = 220$  mW circulating power level at a detuning of 0.35 linewidths, this is equivalent to  $P_{\text{in}} = 31 \mu\text{W}$  incident on the cavity, obtained from the relationship

$$P_{\text{circ}} = \frac{4}{T_i} \times \frac{1}{1 + \delta_\gamma^2} P_{\text{in}} \quad (5)$$

where  $T_i$  is the transmission of the microresonator. The amplitude spectral density for power fluctuations due to shot noise inside the cavity may then be calculated as

$$\tilde{P}_{\text{circ}} = \sqrt{2\hbar\omega_0 P_{\text{in}}} \times \frac{P_{\text{circ}}}{P_{\text{in}}} \quad (6)$$

where  $\omega_0$  is the laser frequency, and the first term is the power spectral density of power fluctuations for the incident light, and the second term accounts for the power amplification in the cavity. The power spectral density for the force on the microresonator is then  $\tilde{F} = 2\tilde{P}_{\text{circ}}/c$ , and the resulting QRPN for frequencies above the mechanical resonance is

$$\tilde{x}_{\text{QRPN}}(\omega) = \frac{2\tilde{P}_{\text{circ}}}{c} \times \chi(\omega) \approx \frac{1}{mc\omega^2} \sqrt{\frac{32\hbar\omega_0 P_{\text{circ}}}{T_i(1 + \delta_\gamma^2)}} \quad (7)$$

where  $\chi(\omega) \approx 1/(m\omega^2)$  is the mechanical susceptibility, and  $\omega$  is the measurement frequency. For our system, we obtain  $x_{\text{QRPN}} \approx 8 \times 10^{-16} \frac{\text{m}}{\sqrt{\text{Hz}}} \times \left[ \frac{\omega}{2\pi \times (10 \text{ kHz})} \right]^{-2}$ , which agrees to within 10% of our full model. Although this calculation was performed without consideration of the optical spring, its effects are removed in our calibration as previously discussed, and it does not modify the ratio of quantum to thermal noise at frequencies below the optical-spring resonance.

In order to observe QRPN, we must make the thermal noise sufficiently small. For the structural damping model that we have found to be consistent with our observed data, given in equation (1), the thermal noise displacement amplitude spectral density scales as  $\omega^{-5/2}$ , whereas the QRPN scales as  $\omega^{-2}$ . This difference indicates that the QRPN will dominate over thermal noise at high frequencies if these scaling laws hold. At frequencies much larger than the fundamental resonance, thermal noise from equation (1) can be approximated to:

$$\tilde{x}_{\text{th}}(\omega) = \sqrt{\frac{4k_B T \omega_m^2}{\omega^5 m Q}} \quad (8)$$

We may then write the ratio of QRPN to thermal noise as:

$$\frac{\tilde{x}_{\text{QRPN}}}{\tilde{x}_{\text{th}}} = \sqrt{\frac{8\hbar\omega_0\omega P_{\text{circ}}}{k_B T m T_i (1 + \delta_\gamma^2)}} \times \frac{1}{\omega_m c} \quad (9)$$

Contrary to traditional cavity optomechanics, a low mechanical resonance frequency is advantageous. This calculation assumes a single mechanical degree of freedom, but as we can see from the measurements, coupling from other modes will also be important. In our system, the scaling law for thermal noise begins to break down at around 30 kHz due to the coupling of the drumhead mode of the microresonator. Despite that limitation, the scaling of thermal noise with frequency is a key factor that allows QRPN to be measured.

**Additional evidence of QRPN.** To provide additional evidence that the displacement noise that we are measuring is a result of QRPN, we perform three more checks. First, we verify that this excess noise is not caused by optical heating of the microresonator. Second, we measure a transfer function from the amplitude modulations going into the cavity to our measurement photodetector  $\text{PD}_M$  and show that the cavity acts as a parametric amplifier. Last, we use the same transfer function to project how much displacement would be caused if the ingoing amplitude fluctuations were shot noise limited.

The effect of bulk heating of the cantilever, which could mimic QRPN, must be ruled out. Owing to the structural damping observed in our device, the mirror motion is dominated by thermal noise below 10 kHz, while still being QRPN-limited above. The low-frequency thermal noise may be used as a thermometer to measure any heating as a result of higher circulating power. To explain the factor of two increase in noise observed at 20 kHz between low and high power as a result of heating, the temperature would have had to increase by a factor of 4. We can rule out this large increase in temperature by observing that the measured noise at frequencies dominated by thermal noise (between 1 kHz and 2 kHz for example) only increases by 2%, which is within measurement uncertainty.

To show that the cavity acts as an optical parametric amplifier, we measure the transfer function of amplitude modulations of the input light to the light detected at  $\text{PD}_M$ . This frequency-dependent transfer function is written as:

$$\text{TF}_{\text{AM}}(\omega) = \frac{\partial P_{\text{PD}_M}}{\partial P_{\text{in}}} \quad (10)$$

To perform this measurement, we modulate the amplitude of the input light using the second amplitude modulator in Fig. 1 and measure the response at  $\text{PD}_M$ . We then perform this measurement again with the cavity unlocked (far from resonance), with the same amount of power incident on  $\text{PD}_M$ . The measurements show that the cavity acts to parametrically amplify the intensity fluctuations incident on the cavity by a constant factor of 4.2 at frequencies below the optical-spring frequency. This parametric amplification is a result of the radiation pressure coupling.

Furthermore, to quantify the displacement noise resulting from this coupling, we multiply  $\text{TF}_{\text{AM}}$  by the shot noise level of the effective input power to the cavity. We then apply our calibration transfer function  $\text{TF}_{\text{cal}}$  to the result to calibrate the displacement noise into units of length. This procedure is outlined in the equations below, where

$$\text{TF}_{\text{cal}}(\omega) = \frac{\partial P_{\text{PD}_M}}{\partial x} \quad (11)$$

is the calibration transfer function, and

$$\tilde{P}_{\text{eff}} = \sqrt{\frac{T_{\text{total}}}{T_i} 2\hbar\omega_0 P_{\text{in}}} \quad (12)$$

is the amount of effective vacuum fluctuations that enter the cavity. The projected displacement noise is calculated as:

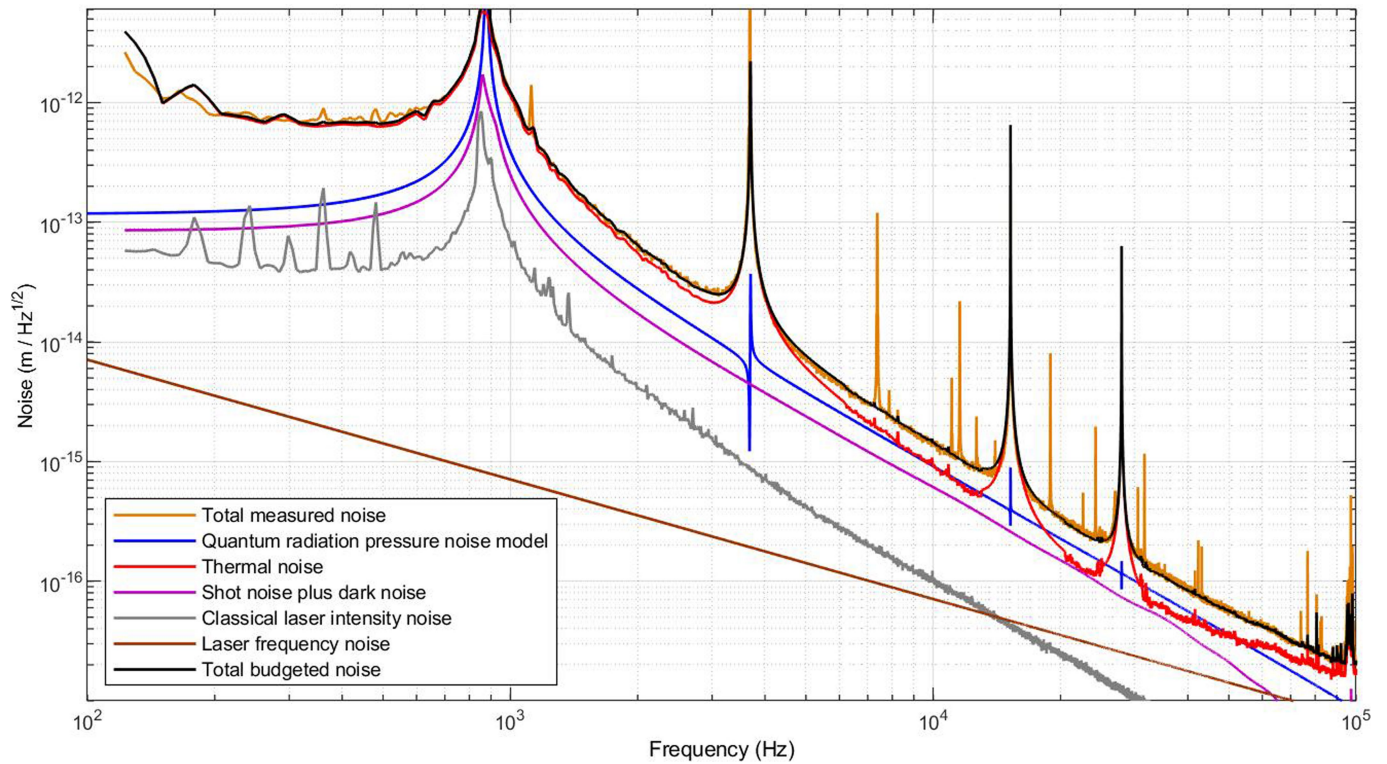
$$\tilde{x}_{\text{projected}}(\omega) = \frac{\tilde{P}_{\text{eff}} \text{TF}_{\text{AM}}}{\text{TF}_{\text{cal}}} \quad (13)$$

The power used to calculate  $\bar{P}_{\text{eff}}$  is scaled from the input power ( $P_{\text{in}}$ ), because the input port only accounts for part of the vacuum fluctuations that enter the cavity; the rest enter from the other cavity losses. This calculation projects the coupling of shot noise to the measurement via radiation pressure on the cantilever. The result of this calculation, shown in Extended Data Fig. 6, agrees with the modelled QRPN, and independently confirms the expected level of QRPN.

### Data availability

The data pertaining to this study are available from the corresponding authors upon reasonable request.

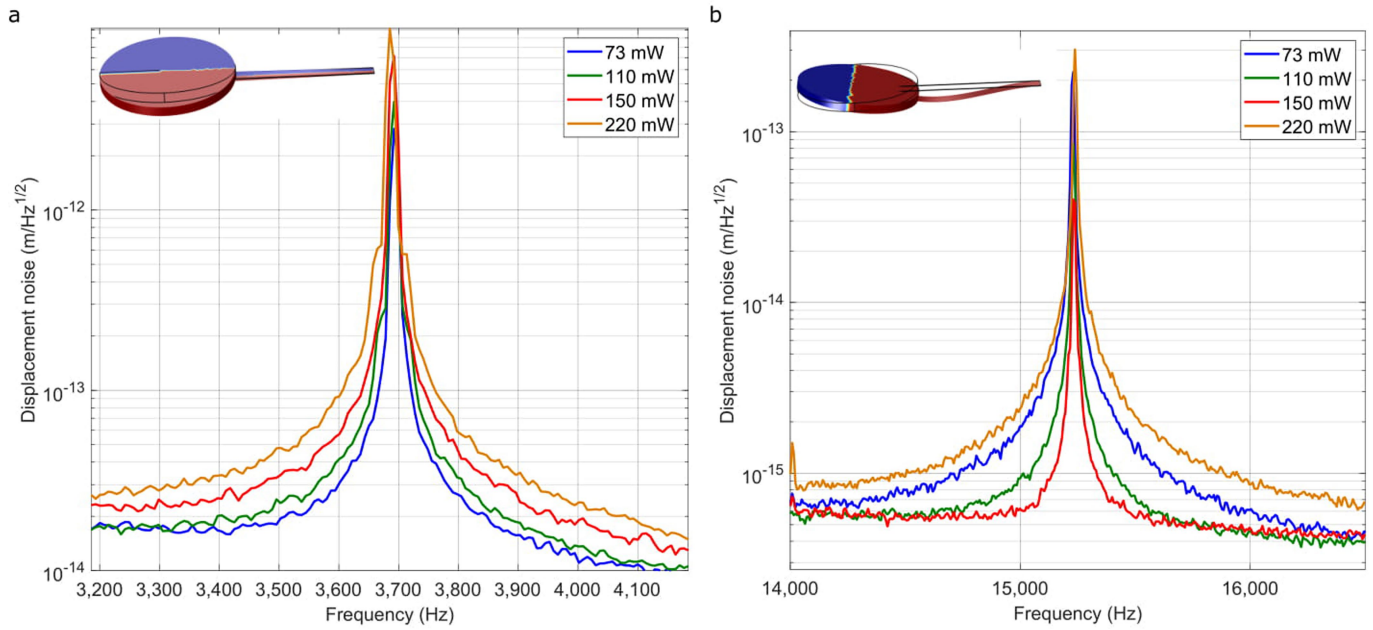
32. Corbitt, T. et al. An all-optical trap for a gram-scale mirror. *Phys. Rev. Lett.* **98**, 150802 (2007).
33. Aspelmeyer, M., Kippenberg, T. J. & Marquardt, F. Cavity optomechanics. *Rev. Mod. Phys.* **86**, 1391–1452 (2014).



**Extended Data Fig. 1 | Full noise budget.** For the measurement with 220 mW circulating power, each noise source that contributed to the sum of subdominant noises in Fig. 2 is shown (see key). The narrow peaks in

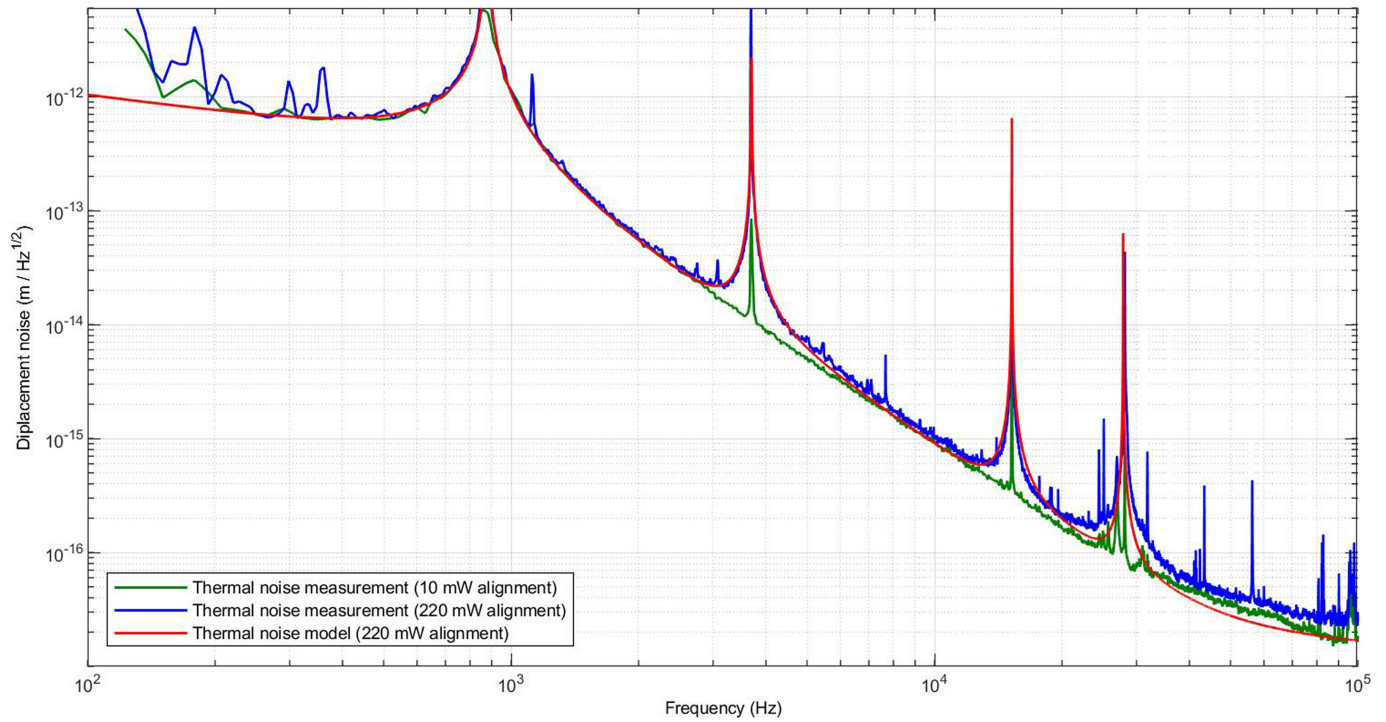
the displacement noise measurement are a result of parametric nonlinear coupling between various mechanical modes, and this coupling is negligible at low circulating powers.





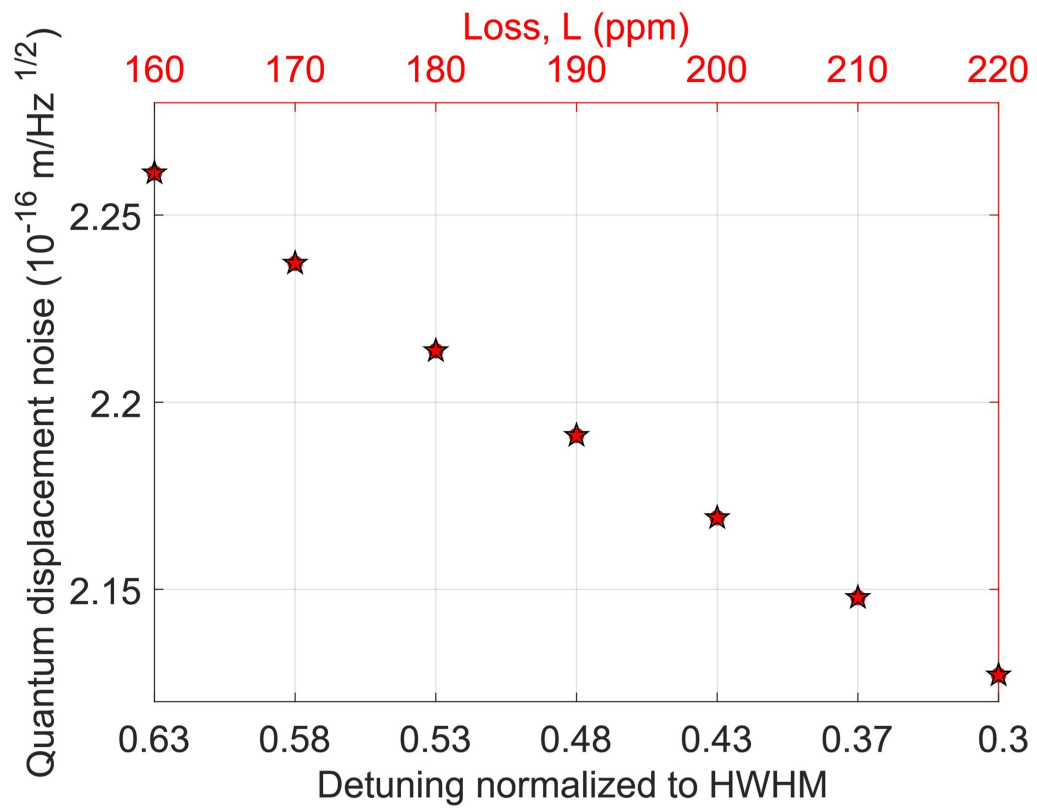
**Extended Data Fig. 2 | Dependence of thermal noise on circulating power as caused by change in beam position.** **a**, The total displacement noise around the yaw mechanical mode for each of the four circulating power levels (see key). **b**, As **a** but centred on the pitch mechanical mode. In these measurements, thermal noise is the dominant noise source at frequencies near the mechanical resonances. The thermal noise around the pitch mode decreases from 73 mW to 110 mW of circulating power,

and then increases at 220 mW. This change is consistent with the cavity mode passing through the nodal point of this mode at an intermediate power level. Each panel includes an image from the finite element model depicting the motion associated with the mechanical mode. In both images, the blue portion represents a positive displacement from equilibrium (thin black outline), and the red area denotes a negative displacement. The nodal line for the mechanical modes is drawn in white.



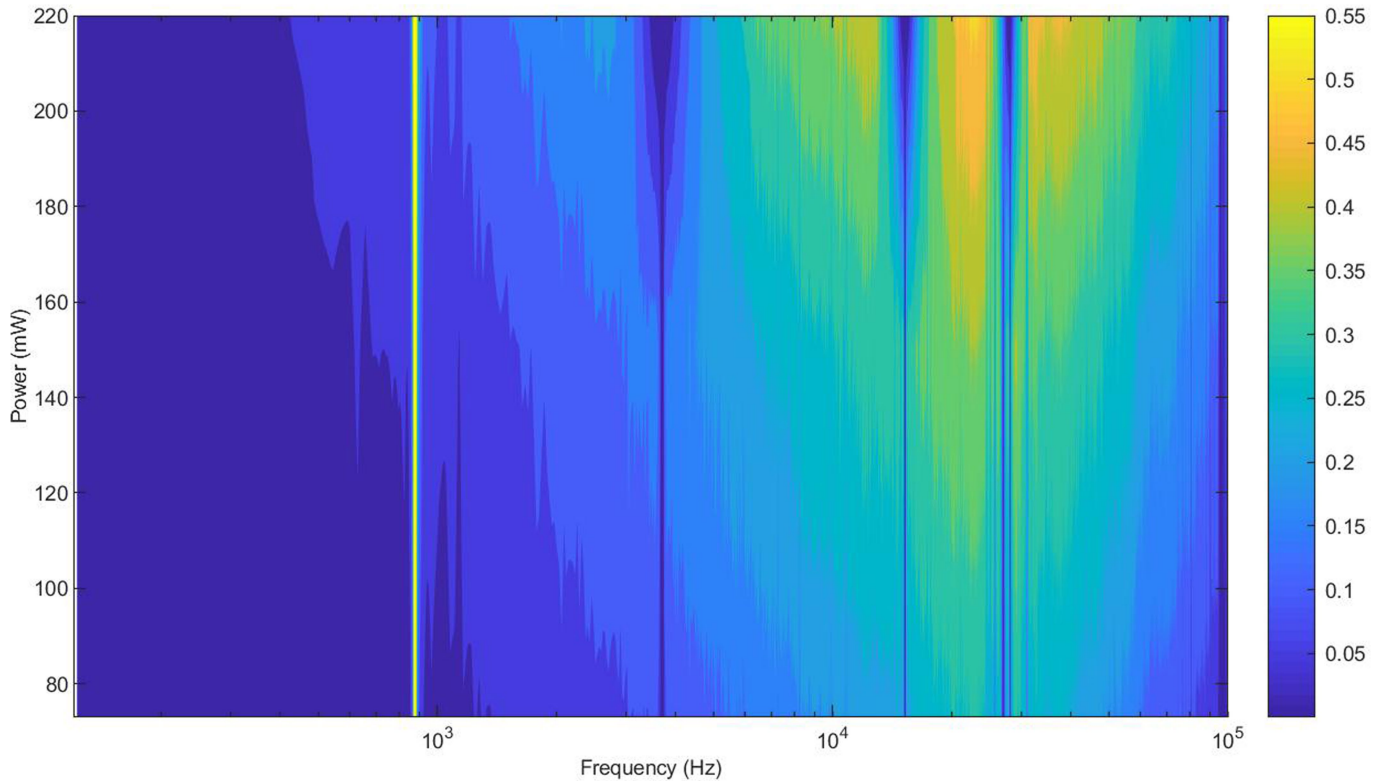
**Extended Data Fig. 3 | Comparison of thermal noise spectra at different alignments.** The effect of the change in beam position is seen in the change of height of the peaks in the displacement spectrum at the frequencies of the higher-order mechanical modes. The blue curve is taken with 10 mW of circulating power with a cavity mode alignment similar to

the QRPN measurement with 220 mW circulating power. The green curve is for an alignment to minimize the coupling of the pitch and yaw modes at 10 mW circulating power. The red curve is based on a model that sets the modal mass of the higher-order modes so that the peaks match those in the displacement measurement shown in Fig. 2.



**Extended Data Fig. 4 | Effect of uncertainty in detuning and loss.** Modelled quantum displacement noise at 20 kHz and 220 mW of circulating power is shown as a function of intracavity loss and cavity detuning: the optical-spring frequency, which has been precisely

measured, is held constant in the model. To be conservative, the range in values for the cavity loss and detuning in this figure are much larger than the constraints obtained by measurements of the optical spring.

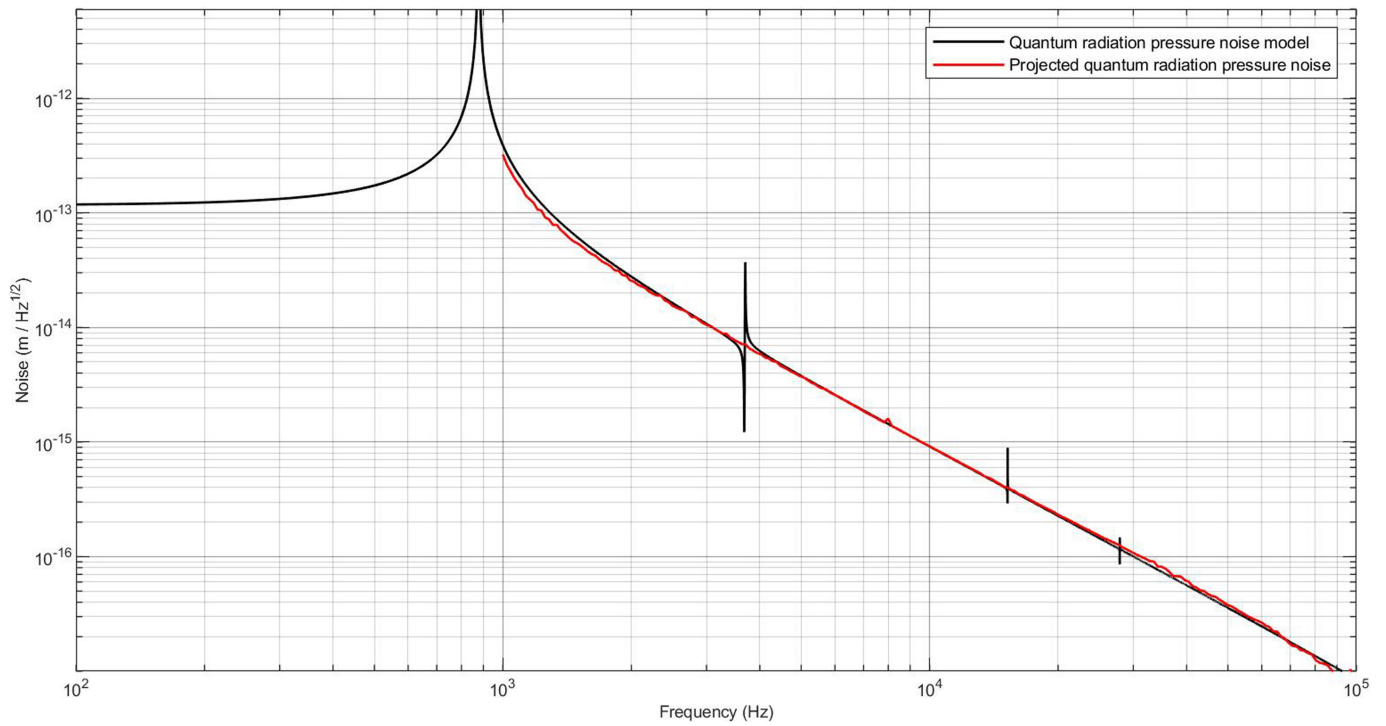


**Extended Data Fig. 5 | QRPN as a function of frequency and power.**

This contour plot shows what fraction of the total measured displacement noise power spectral density (PSD) is contributed by QRPN, as a function of measurement frequency and circulating power. The quantity shown on the colour scale at right is the ratio of the PSDs of the QRPN model to the total measured noise. Whereas in the rest of this Letter we present the data as amplitude spectral densities in order to put them in the perspective of GW measurements, we use PSDs to calculate percentage and ratios, and

to make this figure, because all the noises are added in quadrature to make up the total noise. We interpolate the data between the measurements at 73 mW, 110 mW, 150 mW and 220 mW. The vertical stripe at 876 Hz is an artefact of the fundamental resonance not being perfectly resolved in the measurement. The blue vertical stripes at 3.7 kHz, 15 kHz and 28 kHz are higher-order mechanical modes of the microresonator. The contours are at a spacing of 0.05 (5%).





**Extended Data Fig. 6 | Projected QRPN.** Shown is the measured QRPN level obtained by multiplying the transfer function measurement  $TF_{AM}$  by the shot noise of the effective cavity input power and applying

the calibration procedure, as described in Methods. The result of this calculation agrees with the modelled QRPN.

Extended Data Table 1 | Standard optomechanical parameters

Parameter	Nominal value
Mechanical resonance frequency	$2\pi \times 876$ Hz
Mechanical quality factor	$1.6 \times 10^4$
Mechanical damping rate	$2\pi \times 0.055$ Hz
Cavity decay rate (HWHM)	$\gamma = 2\pi \times 580$ kHz
Laser detuning from cavity resonance	$0.3 - 0.6 \gamma$
Optomechanical single-photon coupling strength	$2\pi \times 380$ kHz
Linearized light-enhanced optomechanical coupling	$2\pi \times 3.5$ MHz
Photon number circulating in cavity	$8 \times 10^7$
Multiphoton cooperativity	$7.4 \times 10^8$
Thermal phonon occupation	$7.4 \times 10^9$

The table shows the measured parameters for our optomechanical system. The parameters in the top half of the table are used in our predictions of noise in the system. The bottom half of the table shows the common optomechanical parameters for comparison with the current state-of-the-art optomechanical systems. As explained in the text, the parameters from the bottom half are typically used to characterize on-resonance systems and are not used in our calculations.